

Multi-scale variation of the meridional movement of the western Pacific warm pool and its associated large-scale climate features

Guojun Zhou^{1,2} · Song Yang^{1,2} · Dawei Zheng³

Received: 13 October 2015 / Accepted: 17 April 2016 / Published online: 4 May 2016
© The Author(s) 2016. This article is published with open access at Springerlink.com

Abstract In this study, we investigated variation of the meridional movement of the western Pacific warm pool (WPWP). The variation was measured by the central latitude (Clat) of the WPWP on various time scales. Its relationships with global sea surface temperature (SST), precipitation, and atmospheric circulation were examined by applying several advanced statistical methods. First, the techniques of wavelet analysis and least-square adjustment were used to depict the time-frequency features and the mean dominant oscillating time scales of the Clat. Then, a multi-stage filtering technique was applied to illustrate the related dominant oscillating signals. We also examined the time-frequency characteristics of the relationships between Clat and the leading modes of the Indo-Pacific oceans by employing a cross-covariance function analysis and a multiple moving-window method. The physical mechanisms for the relationships between Clat and the patterns of SST, precipitation, and atmospheric circulation were discussed. Results indicated that there is a weakening trend in the oscillation of Clat mainly because the quasi-annual oscillation of Clat increases in January–March and decreases in July–September. The semi-annual oscillation of Clat closely interacts with the westerly wind over the summer hemisphere of the tropical western Pacific Ocean and with the easterly wind over the winter hemisphere of the ocean. The interannual

component of Clat corresponds to El Niño–Southern Oscillation and the Indian Ocean basin-wide warming or cooling with strengthened oscillations in the 1970s, and the lower-frequency component of Clat closely corresponds to the central Pacific type of El Niño from the 1990s.

Keywords Multi-scale variation · Western Pacific warm pool · Central latitude · Multi-stage filter

1 Introduction

The meridional displacement of the western Pacific warm pool (WPWP) is one of the most significant features of the warm pool. The WPWP has been identified as the region of warm water in the western tropical Pacific Ocean (PO), where organized deep convective systems transfer heat and moisture from the ocean into the atmosphere, and it serves as a major source of heat and water vapor for large-scale atmospheric circulations (Webster and Lukas 1992; Waliser and Graham 1993). The definition of the WPWP can be categorized as two kinds, based on the features of moving WPWP and fixed WPWP. The moving WPWP is featured by the region of warm pool that varies with its evolution and is defined by isotherms from 27.5 to 29.0 °C in the western tropical PO (Wyrski 1989; Yan et al. 1992; Cravatte et al. 2009; Hoys and Webster 2012). This is because the sea surface temperatures (SSTs) in excess of 27.5 °C are required for large-scale deep convection to occur (Graham and Barnett 1987). The fixed WPWP is a specified area in the western tropical PO, and it does not vary with time (Huang and Sun 1994; Li et al. 1999; Sun 2003). Usually, it is a part of the climate mean state. In the present study, the WPWP refers to the moving WPWP. The establishment of the WPWP is by external forcing, such as solar irradiance variation and volcanic activity (Yan et al. 1992), and by

✉ Song Yang
yangsong3@mail.sysu.edu.cn

¹ School of Atmospheric Sciences, Sun Yat-sen University, 135 West Xingang Road, Guangzhou 510275, China

² Institute of Earth Climate and Environment System, Sun Yat-sen University, Guangzhou, China

³ Center for Astrodynamics Research, Shanghai Astronomical Observatory, Chinese Academy of Sciences, Shanghai, China

internal variability of the atmosphere (Ramanathan and Collins 1991; Wallace 1992; Pierrehumbert 1995), the ocean (Bjerknes 1966; Wyrki 1975), and their interactions (Dijkstra and Neelin 1995; Clement et al. 2005). The meridional displacement of the WPWP is characterized by its most pronounced annual cycle, which is related to the annual march of solar heating; it migrates northward from the boreal winter to summer and southward from the boreal summer to winter (Wyrki 1989; Ho et al. 1995; Kim et al. 2012). Wyrki (1989) suggested that the trade winds also contribute to the fluctuation of the WPWP by coupling with two subtropical gyres. Kim et al. (2012) showed that the latitudinal center of the WPWP is shifted southward during El Niño years and northward during La Niña years, but its correlation with the Niño3.4 index is weak in December–February (DJF). (ENSO) and the WPWP annual cycle generated an atmospheric combination mode (C-mode) of wind variability; therefore, it is inadequate to assess ENSO impact by considering only interannual time scales (Stuecker et al. 2013; Stuecker et al. 2015; Zhang et al. 2015). A number of questions remain, however. What are the features of the meridional movement of the WPWP in different time scales, such as semi-annual, interannual, and interdecadal beside the annual cycle? How are these features related to global climate?

For the location of the WPWP, previous studies usually defined the centroid of the WPWP under the assumption that the WPWP is a homogeneous water mass to represent the evolution of the WPWP (Ho et al. 1995; Picaut et al. 1996; Yan et al. 1997). Other studies (Chen and Fang 2005; Hu and Hu 2012) took the actual SST structure within the WPWP into account and defined the center of heat measured by normalized temperature weighting function to track its horizontal migration. Due to its stronger relationship with ENSO, the zonal displacement of the WPWP is relatively emphasized more than the meridional movement (Picaut et al. 1996, 2001; Bosc et al. 2009; Maes et al. 2010).

Although the meridional movement of the WPWP is predominantly controlled by the annual march of solar heating, and only the annual oscillation signal appears most significantly in power spectral analysis (Ho et al. 1995; Hu and Hu 2012), it seems worthy further uncovering detailed characteristics of multi-scale variation of the meridional movement of the WPWP with advanced tools, especially when the diversity of El Niño (Yeh et al. 2014; Capotondi et al. 2015) has received increasing attention over the last decade because of the frequent emergence of the central Pacific El Niño, which is also called dateline El Niño, El Niño Modoki, or warm pool El Niño (Fu et al. 1986; Larkin and Harrison 2005; Ashok et al. 2007; Kao and Yu 2009; Kug et al. 2009).

In this study, we focus on the meridional displacement of the WPWP by investigating the variation of the central latitude (Clat) of the WPWP. Clat is defined by the temperature-weighted average due to the actually inhomogeneous SST

distribution in the WPWP. We investigate the multi-scale variations of Clat in both time and frequency domains and explore the relationships of the multi-scale oscillations of Clat with global SST, precipitation, and atmospheric circulation. We further depict the time-frequency characteristics of the relationships between Clat and the leading modes of the Indian Ocean (IO) and the PO.

The paper is organized as follows: first, we describe the data sets and methodology in Section 2. We then deal with the characteristics of Clat in both time and frequency domains in Section 3. Detailed relationships of the multi-scale oscillations of Clat with global SST, precipitation, and large-scale atmospheric circulation are given in Section 4. An examination of time-frequency characteristics of the relationships between Clat and the leading modes of the IO and the PO is carried out in Section 5. Finally, we summarize the results in Section 6.

2 Data sets and analysis methods

2.1 Data sets

Two sets of SST data are used: the Improved Extended Reconstructed Sea Surface Temperature version 3b (ERSST V.3b) of the National Oceanic and Atmospheric Administration (NOAA) (Smith et al. 2008) and the UK Met Office Hadley Centre Sea Ice and Sea Surface Temperature data set (HadISST) (Rayner et al. 2003). The ERSST V.3b was constructed and updated by applying the most recently available SST in the International Comprehensive Ocean-Atmosphere Data Set (ICOADS) SST data and using improved statistical methods that allowed for stable reconstruction with sparse data. It covers the time period from January 1854 to present in 2° by 2° global grid provided by the NOAA/OAR/ESRL PSD, Boulder, CO, USA (<http://www.esrl.noaa.gov/psd/>). The HadISST is a combination of global monthly fields of SST and sea ice concentration on 1° by 1° grid from 1870 to present. It was reconstructed by using a two-stage reduced-space optimal interpolation procedure. We extracted SST data from January 1948 to December 2012 and found similar results from the two data sets. Thus, we only present the results from ERSST V.3b in this paper.

The large-scale atmospheric features are analyzed from the National Centers for Environmental Prediction-National Center for Atmospheric Research (NCEP-NCAR) Reanalysis (Kalnay et al. 1996). The data set coverage starts in January 1948 and is continuously updated by the NOAA/OAR/ESRL PSD (<http://www.esrl.noaa.gov/psd/>). To ensure the robustness of our results, we also examined the ERA-40 reanalysis from September 1957 to August 2002 (Uppala et al. 2005) and the ECMWF Interim reanalysis (ERA-Interim), which is a global atmospheric reanalysis from 1979 to present (Dee et al. 2011). We found similar results

from various reanalysis products and, thus, only present the results from the NCEP-NCAR reanalysis (from January 1948 to December 2012). We use the Global Precipitation Climatology Project (GPCP) monthly precipitation data set version 2.2 (Adler et al. 2003) for the period of 1979–2012 at 2.5° by 2.5° global grid provided by the NOAA/OAR/ESRL PSD. We also use the TS (time series) 3.21 data sets from the Climatic Research Unit (CRU) of the University of East Anglia, UK (Harris et al. 2014). It contains land-only data information based on gauge observations for the period of 1901–2012; its resolution is 0.5° by 0.5°. More details of the CRU data set can be found online (<http://www.cru.uea.ac.uk/data/hrg/>).

The central-eastern tropical Pacific SST is represented by the Niño3.4 SST (averaged over 5° S–5° N, 170°–120° W), which has often been used for measuring the conditions of ENSO. El Niño Modoki is identified by the El Niño Modoki Index (EMI) given by Ashok et al. (2007), that is, $EMI = [SSTA]_C - 0.5[SSTA]_E - 0.5[SSTA]_W$, where the square brackets with a subscript represent the area-averaged SST anomalies (SSTAs) over the central Pacific region C (10° S–10° N, 165° E–140° W), the eastern Pacific region E (15° S–5° N, 110°–70° W), and the western Pacific region W (10° S–20° N, 125°–145° E), respectively. The Pacific Decadal Oscillation (PDO) index is defined by Mantua et al. (1997) using the leading principal component of North Pacific monthly SST variability (poleward of 20° N). Digital values of the PDO index are obtained from the website of the Joint Institute for the Study of the Atmosphere and Ocean of the University of Washington at <http://jisao.washington.edu/pdo/PDO.latest>. Following Saji et al. (1999), we define SSTs over the tropical western Indian Ocean (WIO), averaged over 10° S–10° N, 50°–70° E, and eastern Indian Ocean (EIO), averaged over 10° S–0°, 90°–110° E. We define the Indian Ocean Dipole (IOD) as the difference in SST between WIO and EIO (WIO SST minus EIO SST). We define the IO basin-wide (IOBW) warming/cooling index using the SSTA averaged over the tropical IO (20° S–20° N, 40°–100° E).

2.2 Methods of analysis

Following the main procedures in Ding et al. (2002) and Yang et al. (2007), we apply the multi-stage filter (MSF; Zheng and Dong 1986; Luo et al. 1987; Zheng and Luo 1992) to extract different time scale components of Clat.

The dominant oscillation time scales and the time-frequency features of Clat variation are independently investigated by applying wavelet analysis (Morlet et al. 1982) and the least-square method with adjustment of the periodic values step by step (Feng et al. 1978). The leap-step time series analysis (LSTSA) model developed by Zheng et al. (2000) is applied to reduce the edge effects in the MSF and wavelet analysis.

We investigate the relationships of Clat with global SST, precipitation, and wind by testing linear correlations with student's *t* test and carrying out regression analysis with *F* test. In particular, we focus on the features of relationships between tropical Indo-Pacific SST leading modes and Clat in both time and frequency domains, using cross-correlation (Jenkins and Watts 1968), Monte Carlo test (Zhou and Zheng 1999), and multiple moving-window spectral technique (Thomason 1982; Zhou et al. 1998) to calculate the squared coherence spectrum between two variables.

3 Variability of Clat

In this section, the WPWP and Clat are defined and the time-frequency features of Clat variation are investigated. The WPWP is defined by the region where SST is above 28.5 °C within 100° E–130° W to separate it from the warm waters in both eastern PO and IO. Following Chen and Fang (2005) and Hu and Hu (2012), Clat of the WPWP is defined as the temperature-weighted average using Eqs. (1) and (2) given below:

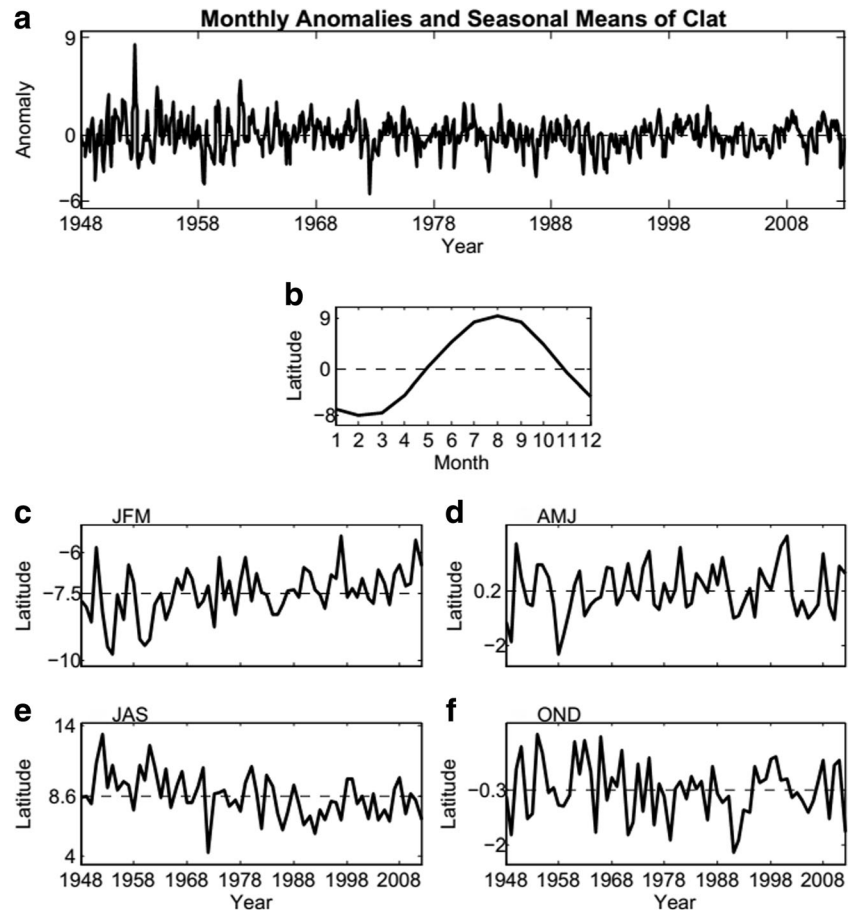
$$\text{Clat}_k = \sum_{i=1}^{n_k} (w_{ik} \times y_{ik}) \quad (1)$$

$$w_{ik} = \frac{T_{ik} - T_{\min,k}}{\sum_{j=1}^{n_k} (T_{jk} - T_{\min,k})} \quad (2)$$

where n_k is the total number of grid points within the WPWP at time k , y_{ik} is the latitude of the i th grid within the WPWP at time k , T_{ik} is the SST of the i th grid within the WPWP at time k , and $T_{\min,k}$ is the minimum SST within the WPWP at time k . $T_{\min,k}$ is usually taken as a constant of the threshold temperature for the WPWP (28.5 °C in this study).

To facilitate discussion, we first show the monthly and seasonal variations of Clat (Fig. 1). Figure 1a illustrates the monthly anomalies in which the long-term-mean annual cycle has been removed. Positive (negative) deviation represents northward (southward) displacement from the mean location, indicating that the monthly fluctuation of Clat weakened after the 1970s. As shown in Fig. 1b, the long-term-mean annual cycle of Clat is affected by the annual march of solar heating, so that the warm pool migrates northward from the boreal winter to summer and reaches the northernmost position about 9° N in August. It shifts southward from the boreal summer to winter, and reaches the southernmost position about 8° S in February. Value of seasonal mean Clat is the highest (about 8.6° N) in July–September (JAS; Fig. 1e), followed by April–June (AMJ), about 0.2° N (Fig. 1d) and October–December (OND), about 0.3° S (Fig. 1f). The smallest value appears in January–March (JFM), about 7.5° S (Fig. 1c). Note that there

Fig. 1 **a** Monthly anomalies of Clat after the long-term-mean annual cycle is removed, **b** the long-term-mean annual cycle, and **c–f** seasonal means of Clat. Units, degree



is an increasing trend in JFM, but a decreasing trend in JAS from the mid 1960s to the late 1990s, indicating that the fluctuation of Clat had weakened since the mid 1960s.

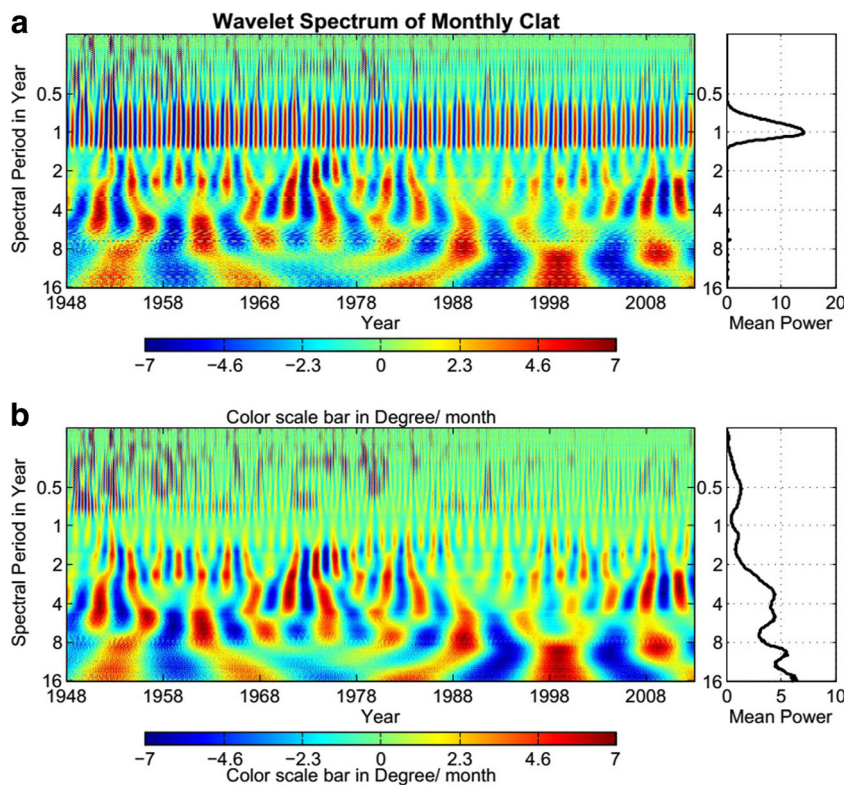
To improve our understanding of the variability of Clat, we perform a more detailed investigation. Figure 2 presents the estimated time-frequency spectrum from the wavelet transform. The variability of Clat is characterized by a predominant annual cycle (see both the amplitude spectrum on the left panel and the mean power on the right panel in Fig. 2a). Figure 2b shows the same features as Fig. 2a, but for Clat without the quasi-annual oscillation. The MSF is applied to filter out the quasi-annual oscillation (in periods of 9–14 months) of Clat before the wavelet transform is applied. In spite of their smaller mean power, apparent signals can be seen on semi-annual, interannual (about 3–6 years), and interdecadal (about 12 years) time scales, indicating that Clat fluctuates as the quasi-biennial oscillation and ENSO as the solar flux variation. Figure 2b also shows that Clat varies, relatively unstably, on non-annual time scales. Semi-annual signals weakened after the 1980s. Interannual signals weakened in the period of the 1960s and 1990s but intensified in the period of the 1970s and 1980s. Interdecadal signals weakened in the period of the 1970s, and intensified from the late 1980s.

After having qualitatively identified the dominant time scales of Clat variation from Fig. 2, we further determine the mean magnitudes and phases of temporal variations of Clat quantitatively by independently applying the least-square method of the Householder transform to the linear regression problem given as follows:

$$Y_t = a_0 + (a_1 \times t) + \sum_{k=1}^4 \left[b_k \times \sin\left(\frac{2\pi \times t}{p_k} + \varphi_k\right) \right] + \varepsilon_t \quad (3)$$

where a_0 and a_1 are constant and linear terms, respectively; b_k , p_k , and φ_k are amplitudes, periods, and phases of the annual, semi-annual, interannual, and interdecadal terms. ε_t is the white noise at time t , whereas the phase estimation is referenced to the epoch of January 1948. Table 1 shows that Clat has the largest amplitude ($8.91^\circ \text{ month}^{-1}$) and the most stable estimate of phases on the annual variation and that it also fluctuates apparently on semi-annual (0.5 years), interannual (3.33 years), and interdecadal (11.33 years) time scales. However, the phases of these fluctuations except for the annual cycle are unstable, with large standard deviations. Table 1 also indicates that there is a decreasing tendency in Clat. The

Fig. 2 *Top left*, estimation of the time-frequency spectra of wavelet transform for Clat. The *red (blue)* color represents positive (negative) amplitude of wavelet spectra. *Top right*, the mean power (dimensionless) of various frequency bands. **b** Same as **a**, except for Clat without the quasi-annual oscillation



root-mean-square (RMS) value of $1.37^{\circ} \text{ month}^{-1}$ is calculated from the residual time series after the constant, linear trend term, and four oscillating signals are removed from the original monthly Clat time series. The constant, linear trend term, and four oscillating signals account for about 97 % of the total RMS of the monthly Clat ($6.47^{\circ} \text{ month}^{-1}$).

We extend our analysis to assess the multi-scale oscillations of Clat variability by applying the MSF to separate the signals in monthly Clat (constant and linear trend removed) for the bands of 0.42–0.58, 0.83–1.17, 3.0–4.5, and 10.0–13.25 years (also refer to Table 1). Figure 3b–e presents the signals for various corresponding time scales: semi-annual,

Table 1 Estimations of the amplitudes and phases of oscillating signals of Clat, ranging from seasonal to interdecadal time scales, derived by the least-square method of the Householder transformation

Row no.	Period (year)	Amplitude ($^{\circ}/\text{month}$)	Phase ($^{\circ}$)
1	0.50	0.452 ± 0.012	-15.91 ± 6.0
2	1.00	8.910 ± 0.078	-148.60 ± 0.2
3	3.33	0.357 ± 0.035	92.07 ± 10.5
4	11.33	0.339 ± 0.067	-95.29 ± 5.0
5	Linear trend	-0.0040 ± 0.00010	
6	RMS	1.3782	

The estimated phases in the table are referenced to the epoch of January 1948

quasi-annual, interannual, and interdecadal, respectively. It can be seen clearly from Fig. 3 that both the wavelet analysis and the MSF consistently indicate that the quasi-annual oscillation (Clat_A) is predominant and that interannual oscillation (Clat_IA) intensified in the period from the late 1960s to the late 1980s but weakened in the 1990s. From the late 1980s, the interdecadal oscillation (Clat_ID) intensified.

To see more detailed features of Clat variation, especially of Clat_A and semi-annual oscillation (Clat_SA), we use Fig. 4 to demonstrate the seasonal means of Clat_SA, Clat_A, Clat_IA, and Clat_ID. In Fig. 4a, c, Clat_SA presents a decreasing trend before the mid 1970s in JFM and JAS. However, Fig. 4b, d shows Clat_SA increased before the mid 1970s in AMJ and OND. These features imply that the oscillation of Clat_SA weakened from the 1950s to the 1970s (also refer to the mean annual cycle of Clat_SA in Fig. 3f). Figure 4e–h indicates the interannual to decadal variations of Clat_A. Before the late 1960s and after the late 1980s, Clat_A presented strong interannual variation and the mean value of Clat_A in JFM increased about 2° from the late 1960s to the late 1980s (see Fig. 4e), while the mean value of Clat_A in JAS decreased by about 2° from the late 1960s to the late 1980s (see Fig. 4g). The high anti-correlation between Clat_A in JFM and that in JAS (correlation coefficient exceeds -0.9) can also be seen from the nearly anti-symmetric feature in Fig. 4e, g as well as between Clat_A in AMJ and that in OND (Fig. 4f, h).

Fig. 3 **a** Monthly Clat and oscillating signals on **b** semi-annual (5–7 months), **c** quasi-annual (10–14 months), **d** interannual (36–54 months), and **e** interdecadal (120–159 months) time scales. **f** The mean semi-annual cycle and **g** quasi-annual cycle of Clat are given at the bottom

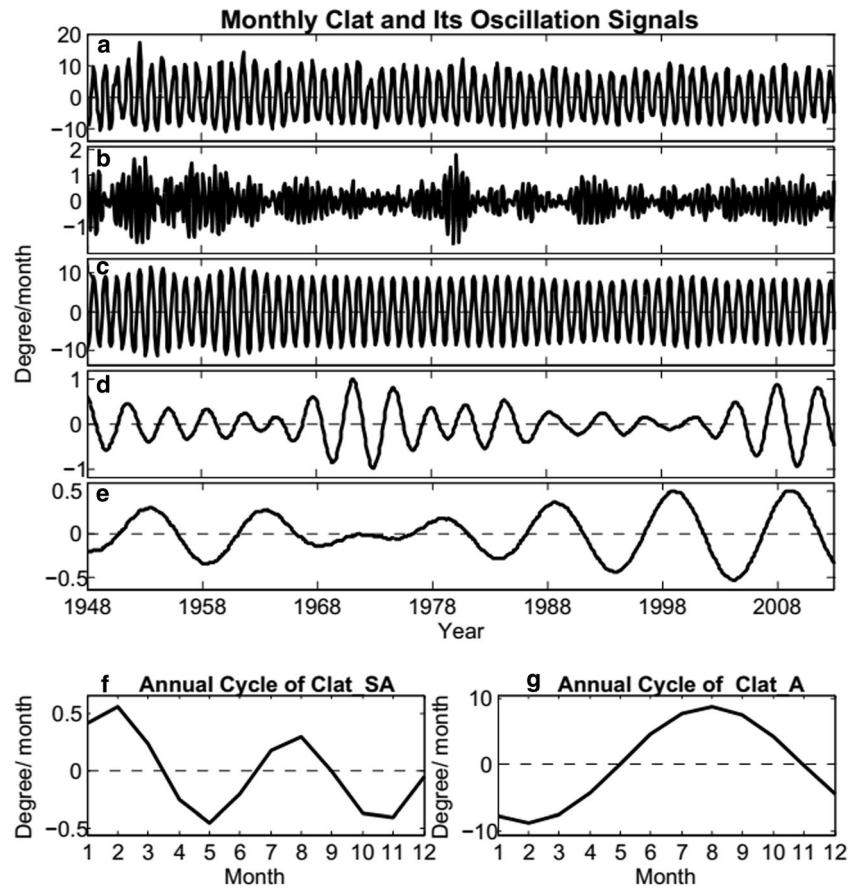
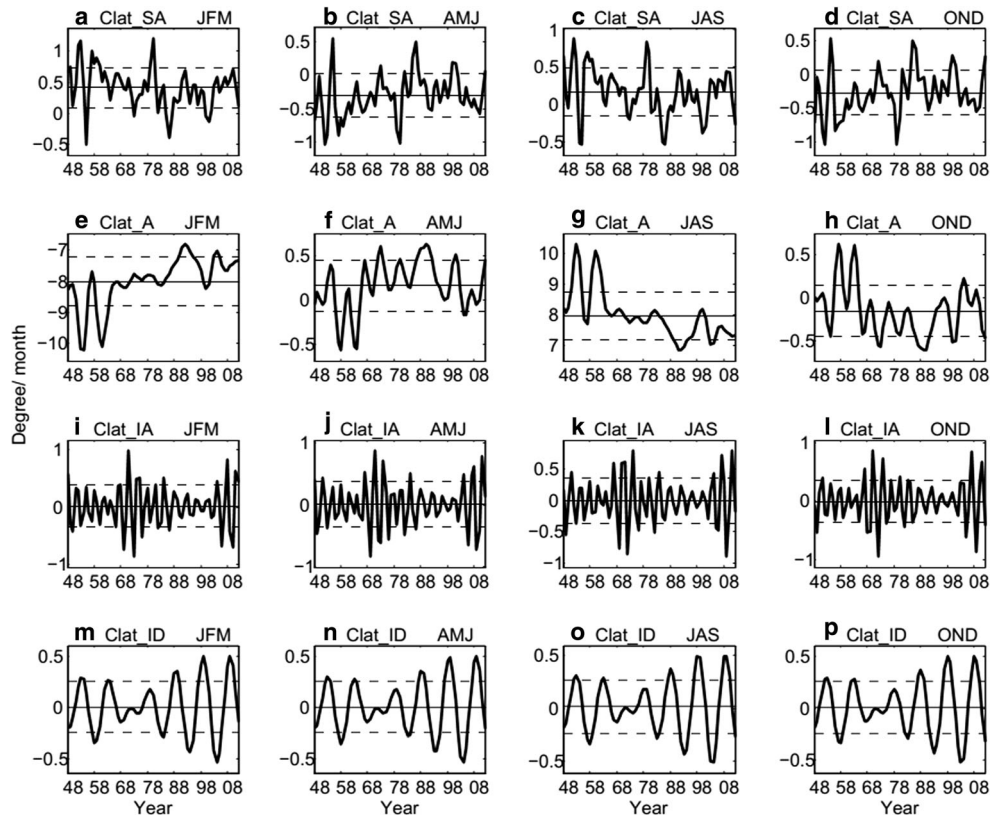


Fig. 4 Seasonal means of semi-annual (**a–d**), quasi-annual (**e–h**), interannual (**i–l**), and interdecadal (**m–p**) components of Clat. The *solid horizontal line* is the climatological mean value, and the *dashed lines* are standard deviations from the climatological mean



4 Large-scale climate patterns associated with Clat variations

To understand the physical mechanism behind Clat and SST relationship, and that behind Clat and precipitation relationship, we analyze the changes in SST, precipitation, and atmospheric circulation patterns associated with the multi-scale components of Clat variations.

Figure 5a shows the correlation between Clat and grid-point SST, superimposed with the regression of 850-hPa wind against Clat, and the correlation between Clat and grid-point precipitation, superimposed with the regression of 200-hPa wind against Clat. They depict the correlation and regression patterns for the period of 1948–2012 when the NCEP-NCAR reanalysis data is available. Only the values significantly above the 95 % confidence level are shown. The SST, precipitation, and atmospheric circulation patterns associated with Clat_SA indicate a coupling between Clat_SA and the combination of the annual march of solar heating and zonal wind over the western equatorial PO. In Fig. 5a, b, the increased SST over the Southern Hemisphere associated with strengthened westerly wind over the southwestern tropical PO and easterly wind over the northwestern tropical PO enhances the precipitation over the southern poleward portion of the WPWP to increase Clat_SA, and vice versa. In Fig. 5e, f, the increased Clat_IA associated with the trade wind over the central-western tropical PO is more strongly intensified than over the central-eastern tropical PO; as a result, divergence appears over the central tropical PO near 150° W to strengthen upwelling and to decrease both SST and precipitation. The westerly wind anomalies over the eastern IO and the Maritime Continent increase Clat_IA via convergence over the western tropical PO near 150° E. In Fig. 5g, h, the increased Clat_ID associated with the trade wind intensifies over the central-western tropical PO and weakens over the central-eastern tropical PO, decreasing SST in the central tropical PO. Note that the SST patterns associated with the increased Clat_IA and Clat_ID are similar in terms of physical mechanisms; the strengthened trade wind over the central-western PO not only accumulates warm water in the western PO, as stated by the Bjerknes feedback in ENSO theory, but also transfers cold water from the eastern PO to increase Clat. Note that the cause of the anomalous atmospheric divergence over the central equatorial PO associated with the increase in Clat_IA is different from that associated with the increase in Clat_ID.

The most significant signals appear in Fig. 5c, d, which shows the changes in SST, precipitation, and atmospheric circulation patterns associated with Clat_A variations. When the WPWP shifts northward, SST warming appears in the Northern Hemisphere and cooling in the Southern Hemisphere. The intensified southwesterly wind over the western IO associated with an increase in Clat_A induces coastal upwelling and enhances surface evaporation cooling in the western Arabian Sea, thereby shrinking warm water to a

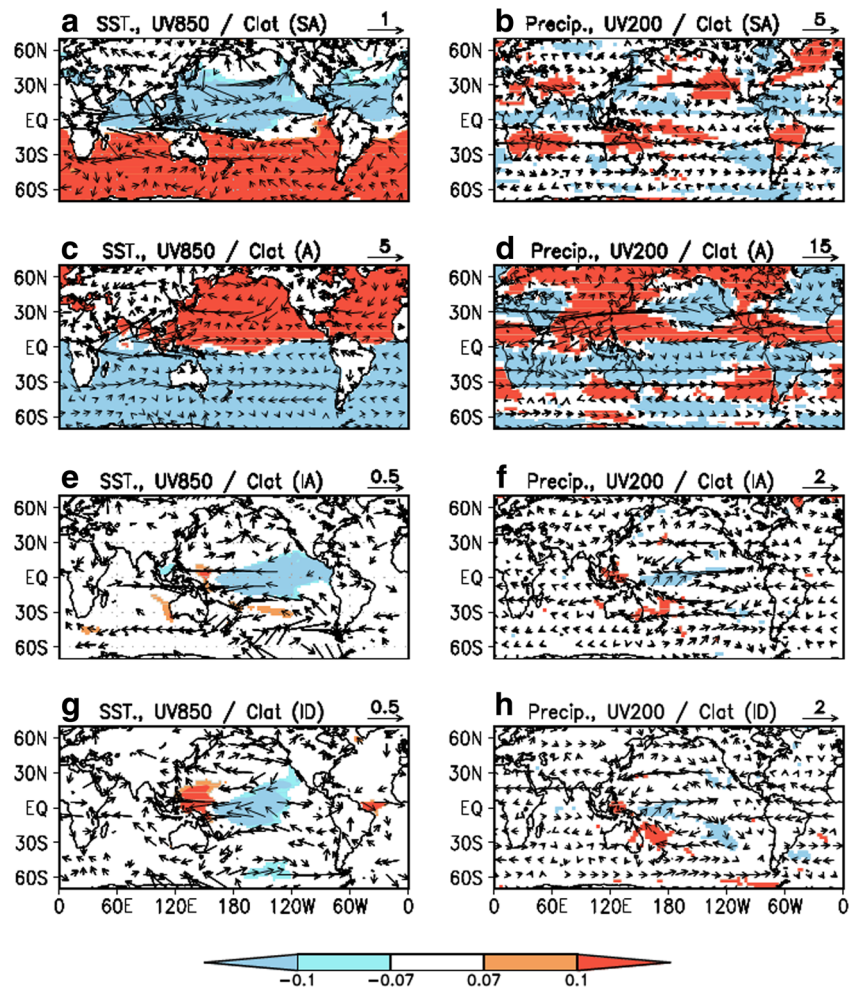
small area in the northeastern corner of the Arabian Sea and the Bay of Bengal (see Fig. 5c). This change in atmospheric circulation also contributes to an increase in precipitation over the Indo-China Peninsula by transporting moisture from the IO to the peninsula (see Fig. 5d). Figure 5c, d also presents increases in precipitation over Japan and eastern China (North America), contributed by the intensified southeasterly wind over the northwestern Pacific (Atlantic) that enhances water vapor supply from the ocean. The strengthened northeasterly wind over the northeastern Pacific enhances upwelling near California and intensifies the subtropical high, and contributes to reduced precipitation in the northeastern Pacific near the west coast of North America.

To further understand climate changes associated with the weakened quasi-annual oscillation of Clat as depicted in Fig. 4e–h, we investigate regressions of SST, precipitation, and 500-hPa omega against Clat_A in different seasons (see Figs. 6, 7, and 8). It is interesting to note that the SST increases over the central equatorial PO (near the dateline) (see Fig. 6) associated with strengthened downstream anomalies in JFM (see Figs. 4e and 8a) with weakened upstream anomalies in JAS (see Figs. 4g and 8c); the precipitation decreases over the Sahel region with weakened upstream anomalies in JAS but increases in northern Australia with strengthened upstream anomalies in JFM (see Fig. 7).

5 Relationships between Clat and dominant Indo-Pacific climate modes

We first examine the relationships between Clat and the leading modes of Pacific-Indian Oceans by analyzing the cross-correlation function in time domain and the squared coherence spectrum in frequency domain. Note that the constant and linear trend terms and the long-term-mean annual cycles have been removed from the Clat and various PO and IO SST indices. Figure 9a–e presents significant correlations between Clat and Niño3.4 SST, EMI, PDO, IOBW, and IOD for the period of 1948–2012, respectively. In the figure, negative lags represent the correlations in which Clat leads the PO and IO SST indices. The correlation is the strongest when Clat leads Niño3.4 SST by 1 month, indicating Clat increases in La Niña years and decreases in El Niño years (see Fig. 9a). Simultaneously, Fig. 9b–e illustrates that the most significant correlation occurs when Clat leads the EMI by 4 months ($R = -0.24$), lags the PDO by 0 months ($R = -0.20$), leads the IOBW by 1 month ($R = -0.19$), and lags the IOD by 20 months ($R = 0.15$). Figure 9f–j illustrates the relationships of Clat with Niño3.4 SST, EMI, PDO, IOBW, and IOD, measured by coherence as a function of frequency bands. A strong relationship is seen between Clat and Niño3.4 SST on the time scales of 2–5 years. The largest coherence spectral peaks occur on interannual time scales, significantly exceeding the

Fig. 5 **a** Patterns of correlations between the semi-annual component of Clat and grid-point SST, and regression of 850-hPa wind (vectors, ms^{-1}) against the semi-annual component of Clat for 1948–2012. **b** Same as **a**, except that SST is replaced by precipitation. **c–d**, **e–f**, and **g–h** are the same as **a–b**, except for quasi-annual, interannual, and interdecadal components of Clat, respectively. Only the correlation coefficients significantly above the 95 % confidence level and winds larger than 0.1 ms^{-1} are shown



threshold value of 0.50 at the 99 % confidence level. A strong relationship is also found between Clat and IOBW in the frequency band of 3–4 years. The relationships of Clat with EMI, PDO, and IOD are relatively less significant.

Because the cross-correlation and cross-coherence are unable to depict the stability and variability of the features in specific frequency bands with respect to time span, we apply the multiple moving-window spectrum technique with subseries of 10 years to investigate coherence features between Clat and the PO and IO SST indices in both time and frequency domains. Figure 10a–e illustrates the distributions of coherence between Clat and the Niño3.4 SST, EMI, PDO, IOBW, and IOD indices in both time (1953–2007) and frequency (bands up to 3 cycles per year) domains. The 99 % confidence level of coherence estimate is shown by a dotted line in the color bar on the right-hand side of each panel. Figure 10a reveals that a highly significant relationship between Clat and Niño3.4 SST exists on the frequency band of about 2–5 years in the period of 1960s–1980s. One of the important features shown in Fig. 10a is that the significance of the Clat–Niño3.4 relationship shifts depending on different frequency

bands in different decades. Figure 10b indicates that a strong relationship between Clat and EMI appears in relatively lower-frequency bands up to 0.5 cycle per year, especially on interannual time scales since the late 1980s. It can be seen by comparing Fig. 10a with Fig. 10b that Clat was more strongly linked to the Niño3.4 SST than to the EMI during the period of 1968–1988, but the relationship between Clat and EMI was more significant than that between Clat and Niño3.4 SST since the late 1980s. This may be because more frequent central Pacific EI Niño events occurred in recent decades (Ren et al. 2013; Yeh et al. 2014). The significant relationship between Clat and PDO appeared in the interdecadal frequency bands in the early 1960s and since 2003 (see Fig. 10c). Figure 10d presents that a highly significant relationship between Clat and IOBW also existed on the frequency band of about 2–5 years in 1968–1978. The coherence between Clat and IOD is large in a wide range of frequency bands, from intraseasonal to interdecadal.

To understand the physical mechanisms for the above-depicted relationships between Clat and the leading modes of PO SST, we analyze the changes in SST and atmospheric

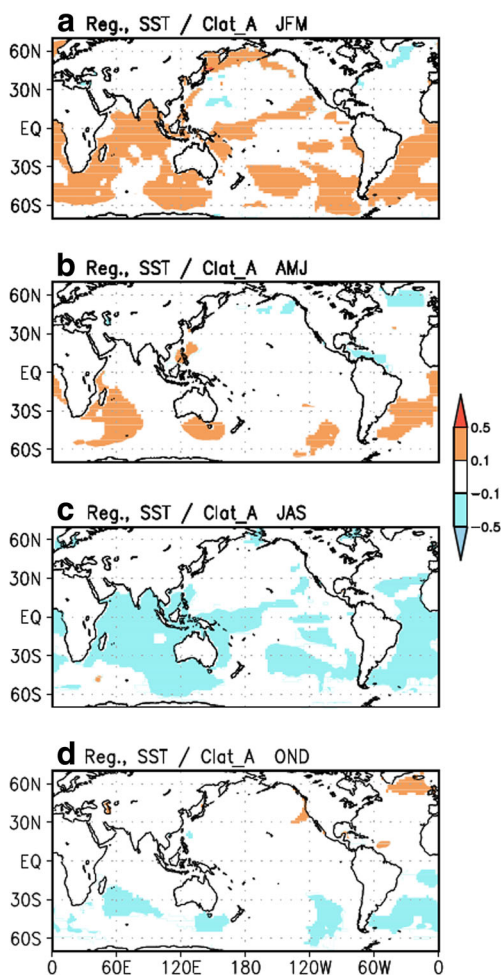


Fig. 6 a Regression patterns of grid-point SST ($^{\circ}\text{C mon}^{-1}$) against the quasi-annual component of Clat in JFM for 1948–2012. Only the values significantly above the 95 % confidence level are shown. **b–d** are the same as **a**, except for AMJ, JAS, and OND, respectively

circulation patterns associated with Clat, Niño3.4 SST, and EMI variations in different times and frequency domains. We examine the correlation between grid-point SST and the interannual component (17–40 months) of Clat, superimposed with the regression of 850-hPa wind against the interannual component of Clat for the periods of 1958–1968 (Fig. 11a) and 1968–1978 (Fig. 11b). Similarly, we also analyze the features for Niño3.4 SST (Fig. 11c, d). Compared with the period of 1958–1968 (Fig. 11a, c), the increased Clat in 1968–1978 (Fig. 11b, d) intensified the SST gradient between the northwestern tropical PO and the southeastern tropical PO, strengthening the southeasterly trade wind over the central-eastern PO, intensified upwelling and evaporation, decreased Niño3.4 SST, and pushed cold water westward, further increasing Clat. The increased Clat and decreased Niño3.4 were also associated with westerly wind anomalies over the eastern equatorial IO and the Maritime Continent and with the cross-equatorial wind anomalies (Fig. 11b, d). The westerly wind anomalies over the eastern equatorial IO and the Maritime Continent as well as the cross-equatorial wind

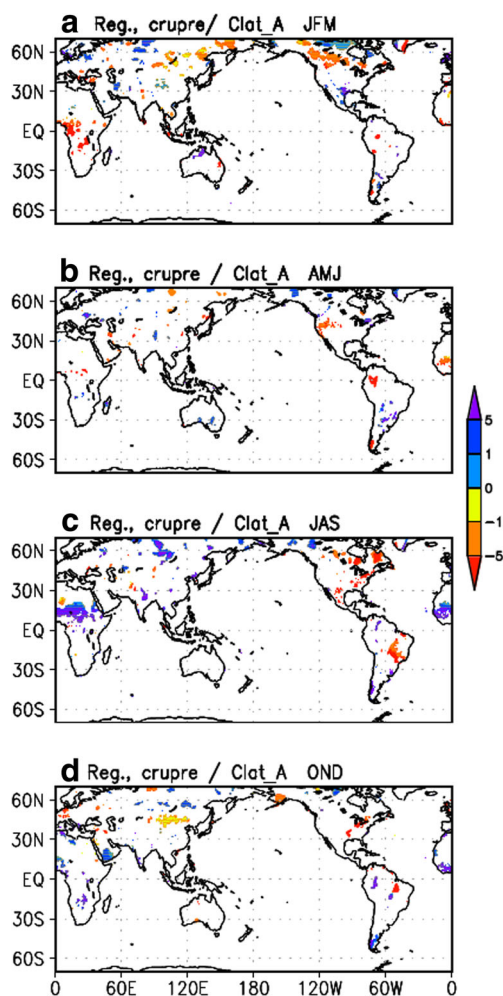


Fig. 7 a Regression patterns of grid-point precipitation (mm mon^{-1}) against the quasi-annual component of Clat in JFM for 1948–2012. Only the values significantly above the 95 % confidence level are shown. **b–d** are the same as **a**, except for AMJ, JAS, and OND, respectively

anomalies contribute to the enhancement of convection over the southern western tropical PO, suppress further westward transport of cold water induced by the strengthened southeasterly trade wind, decrease Clat, and decrease the SST gradient between the northwestern tropical PO and the southeastern tropical PO to weaken the southeasterly trade wind over the central-eastern PO, increasing Niño3.4 SST (Fig. 11b, d). As a result, both Clat and Niño3.4 SST are closely (negatively) related to each other. We want to emphasize that both the southeasterly trade wind anomalies over the central-eastern PO and the westerly wind anomalies over the eastern equatorial IO and the Maritime Continent are essential for the significantly higher coherence between the interannual components of Clat and Niño3.4 SST.

We further investigate the correlation between grid-point SST and the lower-frequency band component (40–120 months) of Clat, superimposed with the regression of 850-hPa wind against the lower-frequency band component of Clat for the periods of 1968–1988 (Fig. 12a) and 1988–

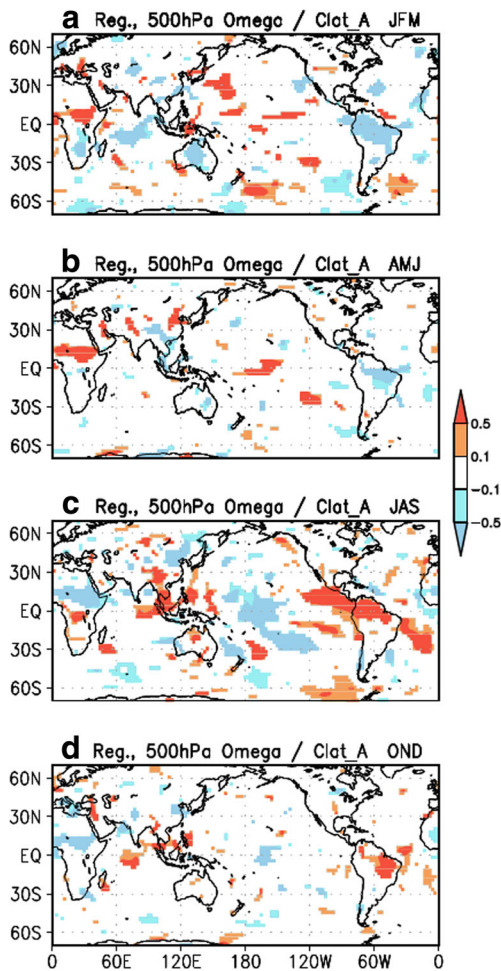


Fig. 8 a Regression patterns of grid-point 500-hPa omega (Pa/100 s) against the quasi-annual component of Clat in JFM for 1948–2012. Only the values significantly above the 95 % confidence level are shown. b–d are the same as a, except for AMJ, JAS, and OND, respectively

2007 (Fig. 12b). Similarly, we also analyze the features for the EMI (Fig. 12c, d) and Nino3.4 SST (Fig. 12e, f). In the relatively lower-frequency band, it is noted that the westerly wind anomalies over the eastern tropical IO, the cross-equatorial wind anomalies, and the northeasterly wind anomalies over the northeastern PO together with the southeasterly wind anomalies over the southeastern PO contribute to the higher coherence between Clat and EMI and to the higher coherence between Clat and Nino3.4 SST. Compared with the period of 1968–1988 (Fig. 12a, c, e), the increased Clat in 1988–2007 (Fig. 12b, d, f) intensified the SST gradient between the northwestern tropical PO and the central equatorial PO, strengthening the trade wind over the central equatorial PO, the northeasterly wind over the northeastern PO, and the southeasterly wind over the southeastern PO. These features lead to the intensification of the two subtropical gyres and transport of cold water from the subtropical PO to the central equatorial PO, referred to as the Pacific Meridional Mode (Chiang and

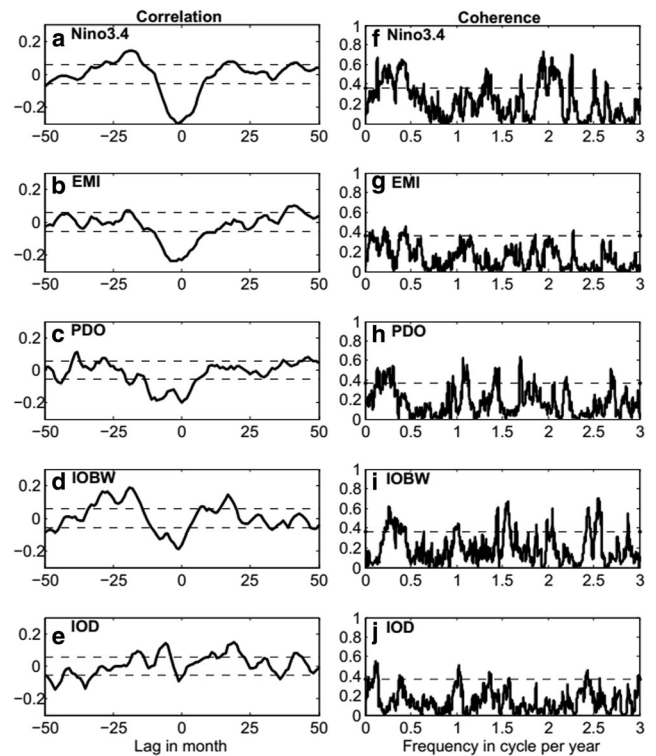


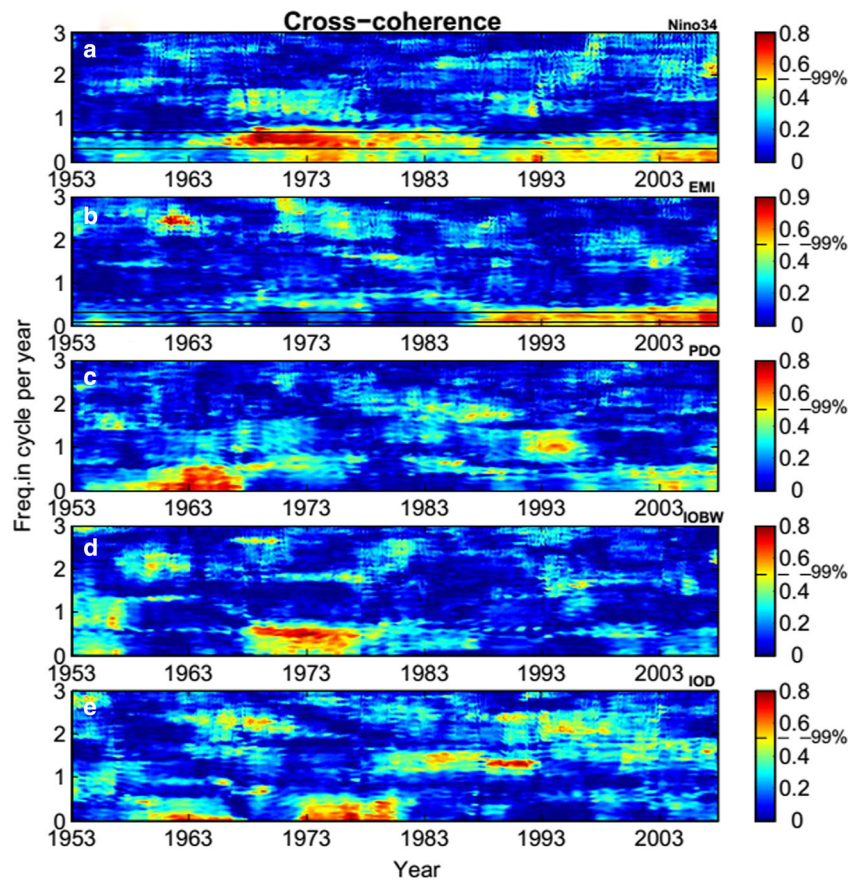
Fig. 9 a–j Estimated cross-correlation (left panels) and squared coherence (right panels; calculated by multi-window spectrum technique) of Clat and Nino3.4 SST, EMI, PDO, IOBW, and IOD. Negative (positive) lags shown in the x-coordinate of each panel represent the correlations in which Clat leads (lags) the Nino3.4 SST, EMI, or PDO. Dotted lines show the threshold values of the significance test at the 95 % confidence level

Vimont 2004; Lin et al. 2015; Yu et al. 2015), and decrease in SST over the equatorial central-eastern PO. As a result, the SST gradient between the northwestern tropical PO and the central equatorial PO further increases (Fig. 12b, d, f). The westerly wind anomalies over the eastern tropical IO and the cross-equatorial wind anomalies associated with the increase in Clat, as discussed above (Fig. 11b, d), contribute to enhanced convection over the southwestern equatorial PO to suppress further increase of Clat, weakening the trade wind, and increase SST over the central tropical PO (Fig. 12b, f).

6 Summary

In this study, we applied several advanced statistical tools to understand the characteristics of multi-scale variations of the WPWP measured by meridional movement of the WPWP or Clat. We first used techniques of wavelet analysis and least-square adjustment to depict the time-frequency features and the mean dominant oscillation time scales of Clat variations and then used a MSF to demonstrate the multi-scale oscillating signals of Clat. We also analyzed SST, precipitation, and atmospheric

Fig. 10 Estimations of coherence spectra (calculated by moving multi-window spectrum technique) between Clat and Nino3.4 SST (a), EMI (b), PDO (c), IOBW (d), and IOD (e) shown in the time-frequency domain. The threshold value of significance test (*F* test) at the 99 % confidence level is indicated by the dashed line in the color legend. Note that a 5-year truncation occurs at the end of the panel. Annual cycle has been removed from each index before the calculation



circulation patterns to understand the physics of the relationships between Clat and global climate. Furthermore, we studied the relationships between Clat and the leading modes of the Indo-Pacific with a focus on the time-frequency characteristics of their coherence by employing a cross-covariance function analysis and a multiple moving-window method.

Among the time scales examined (ranging from semi-annual to interdecadal) for Clat variations, the quasi-annual and semi-annual signals, especially the former, have the most stable oscillating frequencies and the largest amplitudes, even if the amplitudes were reduced by about 2° from the late 1960s to the late 1980s because of the Clat_A decrease in JFM and increase in JAS. The non-seasonal signals (on semi-annual,

Fig. 11 a Correlation between grid-point SST and the interannual (17–40 months) component of Clat, superimposed with the regression of 850-hPa wind against the interannual (17–40 months) component of Clat in the period of 1958–1968. b Same as a, except for the period of 1968–1978. c–d Same as a–b, except for Nino3.4 SST. Only the correlation coefficients significantly above the 95 % confidence level and winds larger than 0.5 ms⁻¹ are shown

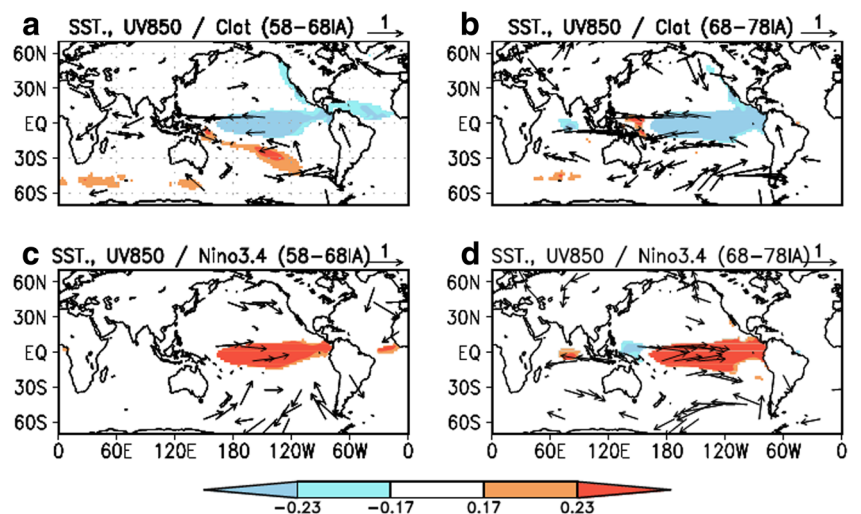
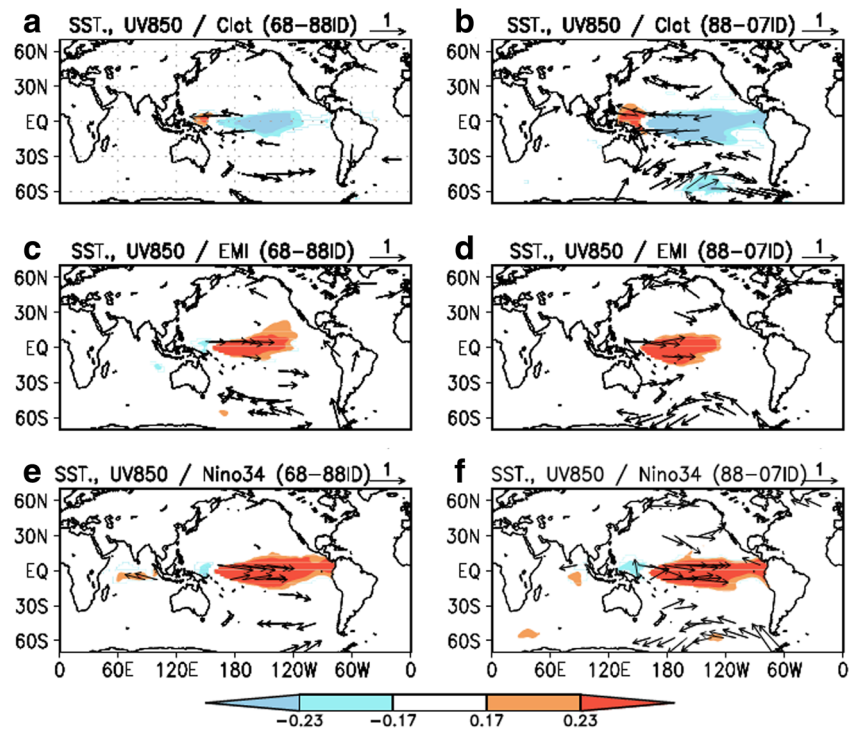


Fig. 12 **a** Correlation between grid-point SST and the lower-frequency band (40–120 months) component of Clat, superimposed with the regression of 850-hPa wind against the lower-frequency band (40–120 months) component of Clat in the period of 1968–1988. **b** Same as **a**, except for the period of 1988–2007. **c–d** and **e–f** are the same as **a–b**, except for EMI and Niño3.4 SST, respectively. Only the correlation coefficients significantly above the 95 % confidence level and winds larger than 0.5 ms^{-1} are shown



interannual, and interdecadal time scales) have smaller amplitudes and more variable frequencies with time. In particular, the interannual oscillation intensified from the late 1960s to the late 1980s and became weaker in the 1990s. The interdecadal oscillation strengthened from the late 1980s. The global SST and atmospheric circulation patterns associated with Clat_SA are nearly opposite to those with Clat_A. This is mainly because the increased SST over the summer hemisphere (associated with strengthened westerly wind over the summer hemisphere of the western equatorial PO and easterly wind over the winter hemisphere of western equatorial PO) enhances the precipitation over the poleward portion of the WPWP to increase the Clat_SA, especially in JFM.

Clat was significantly correlated with Niño3.4 SST and IOBW on the frequency band of about 2–5 years during the 1960s–1980s when the quasi-biannual oscillation of Clat intensified. The strengthened southeasterly trade wind over the central-eastern PO enhanced upwelling in the eastern equatorial PO, and Niño3.4 SST decreased associated with the increase in the quasi-biannual oscillation of Clat. Meanwhile, divergence appeared near 150° W because of the difference in the trade wind. The westerly wind anomalies over the central-eastern IO associated with the increase in the biannual oscillation of Clat contributed to an IO basin-wide cooling by strengthening the upwelling and evaporation over the IO and to the convection with intensified trade wind over the western PO, increasing the SST over the western equatorial PO near 150° E . Since the late 1980s, a strong relationship between Clat and EMI appeared in a relatively lower-frequency band of about 4–10 years. The trade wind strengthened over the

central-western PO but weakened over the central-eastern PO. The divergence near 150° W enhanced upwelling in the central PO, and EMI decreased associated with the increase in the interannual oscillation of Clat, further inducing southwesterly wind anomaly over the northern central equatorial PO to form the Pacific Meridional Mode.

Acknowledgments The study was jointly supported by the National Key Research Program of China (Grant 2014CB953900), the National Natural Science Foundation of China (Grant 41375081), China Special Fund for Meteorological Research in the Public Interest (No. GYHY201406018), the Special Funds of Guangdong Province of China (No. YCJ2013-196), and the Jiangsu Collaborative Innovation Center for Climate Change and the Zhuhai Joint Innovative Center for Climate, Environment and Ecosystem of China.

Open Access This article is distributed under the terms of the Creative Commons Attribution 4.0 International License (<http://creativecommons.org/licenses/by/4.0/>), which permits unrestricted use, distribution, and reproduction in any medium, provided you give appropriate credit to the original author(s) and the source, provide a link to the Creative Commons license, and indicate if changes were made.

References

- Adler RF, Huffman GJ, Chang A, Ferraro R, Xie PP, Janowiak J, Rudolf B, Schneider U, Curtis S, Bolvin D, Gruber A, Susskind J, Arkin P, Nelkin E (2003) The version-2 Global Precipitation Climatology Project (GPCP) monthly precipitation analysis (1979–present). *J Hydrometeorol* 4:1147–1167
- Ashok K, Behera SK, Rao SA, Weng HY, Yamagata T (2007) El Niño Modoki and its possible teleconnection. *J Geophys Res* 112: C11007. doi:10.1029/2006JC003798

- Bjerknes J (1966) A possible response of the atmospheric Hadley circulation to equatorial anomalies of ocean temperature. *Tellus* 18:820–829
- Bosc C, Delcroix T, Maes C (2009) Barrier layer variability in the western Pacific warm pool from 2000 to 2007. *J Geophys Res* 114:C06023. doi:10.1029/2008JC005187
- Capotondi A, Wittenberg AT, Newman M, Lorenzo ED, Yu JY, Braconnot P, Cole J, Dewitte B, Giese B, Guilyardi E, Jin FF, Karnauskas K, Kirtman B, Lee T, Schneider N, Xue Y, Yeh SW (2015) Understanding ENSO diversity. *Bull Amer Meteorol Soc* 96:921–938
- Chen G, Fang LX (2005) Improved scheme for determining the thermal centroid of the oceanic warm pool using sea surface temperature data. *J Oceanogr* 61:295–299
- Chiang JCH, Vimont DJ (2004) Analogous Pacific and Atlantic meridional modes of tropical atmosphere-ocean variability. *J Clim* 17:4143–4158. doi:10.1175/JCLI4953.1
- Clement AC, Seager R, Murtugudde R (2005) Why are there tropical warm pools? *J Clim* 18:5294–5311
- Cravatte S, Delcroix T, Zhang DX, McPhaden M, Leloup J (2009) Observed freshening and warming of the western Pacific warm pool. *Clim Dyn* 33:565–589. doi:10.1007/s00382-009-0526-7
- Dee DP, Uppala SM, Simmons AJ, Berrisford P, Poli P, Kobayashi S, Andrae U, Balmaseda MA, Balsamo G, Bauer P, Bechtold P, Beljaars ACM, Berg LVD, Bidlot J, Bormann N, Delsol C, Dragani R, Fuentes M, Geer AJ, Haimberger L, Healy SB, Hersbach H, Hólm EV, Isaksen I, Kållberg P, Köhler M, Matricardi M, McNally AP, Monge-Sanz BM, Morcrette JJ, Park BK, Peubey C, Rosnay PD, Tavolato C, Thépaut JN, Vitart F (2011) The ERA-interim reanalysis: configuration and performance of the data assimilation system. *Q J R Meteorol Soc* 137:553–597. doi:10.1002/qj.828
- Dijkstra HA, Neelin JD (1995) Ocean-atmosphere interaction and the tropical climatology. Part II: why the Pacific cold tongue is in the east. *J Clim* 8:1343–1359
- Ding XL, Zheng DW, Yang S (2002) Variations of the surface temperature in Hong Kong during the last century. *Int J Climatol* 22:715–730. doi:10.1002/joc.760
- Feng K, Zhang J, Zhang Y, Yang Z, Chao W (1978) The numerical calculation method. National Defense Industry Press, 311 pp (in Chinese)
- Fu CB, Diaz HF, Fletcher JO (1986) Characteristics of the response of sea surface temperature in the central Pacific associated with the warm episodes of the Southern Oscillation. *Mon Weather Rev* 114:1716–1738
- Graham NE, Barnett TP (1987) Sea surface temperature, surface wind divergence, and convection over tropical oceans. *Science* 238:657–659. doi:10.1126/science.238.4827.657
- Harris I, Jones PD, Osborn TJ, Lister DH (2014) Updated high-resolution grids of monthly climatic observations—the CRU TS3.10 Dataset. *Int J Climatol* 34:623–642. doi:10.1002/joc.3711
- Ho CR, Yan XH, Zheng QA (1995) Satellite observations of upper-layer variabilities in the western Pacific warm pool. *Bull Amer Meteorol Soc* 76:669–679
- Hoys CD, Webster PJ (2012) Evolution and modulation of tropical heating from the last glacial maximum through the twenty-first century. *Clim Dyn* 38:1501–1519. doi:10.1007/s00382-011-1181-3
- Hu SJ, Hu DX (2012) Heat center of the western Pacific warm pool. *Chin J Oceanol Limnol* 30:169–176. doi:10.1007/s00343-012-1193-9
- Huang RH, Sun FY (1994) Impact of the convective activities over the western tropical Pacific warm pool on the intraseasonal variability of the East Asian summer monsoon. *Scientia Atmospherica Sinica* 18:456–465 (in Chinese)
- Jenkins G, Watts D (1968) *Spectrum analysis and its applications*. Holden-Day, San Francisco, CA 525 pp
- Kalnay E, Kanamitsu M, Kistler R, Collins W, Deaven D, Gandin L, Iredell M, Saha S, White G, Woollen J, Zhu Y, Chelliah M, Ebisuzaki W, Higgins W, Janowiak J, Mo KC, Ropelewski C, Wang J, Leetmaa A, Reynolds R, Jenne R, Joseph D (1996) The NCEP/NCAR 40-year reanalysis project. *Bull Amer Meteorol Soc* 77:437–471
- Kao HY, Yu JY (2009) Contrasting eastern-Pacific and central-Pacific types of ENSO. *J Clim* 22:615–632. doi:10.1175/2008JCLI2309.1
- Kim ST, Yu JY, Lu MM (2012) The distinct behaviors of Pacific and Indian Ocean warm pool properties on seasonal and interannual time scales. *J Geophys Res* 117:D05128. doi:10.1029/2011JD016557
- Kug JS, Jin FF, An SI (2009) Two types of El Niño events: cold tongue El Niño and warm pool El Niño. *J Clim* 22:1499–1515. doi:10.1175/2008JCLI2624.1
- Larkin NK, Harrison DE (2005) Global seasonal temperature and precipitation anomalies during El Niño autumn and winter. *Geophys Res Lett* 32:L16705. doi:10.1029/2005GL022860
- Li CY, Mu MQ, Zhou GQ (1999) The variation of warm pool in the equatorial western Pacific and its impacts on climate. *Adv Atmos Sci* 16:378–394
- Lin CY, Yu JY, Hsu HH (2015) CMIP5 model simulations of the Pacific meridional mode and its connection to the two types of ENSO. *Int J Climatol* 35:2352–2358. doi:10.1002/joc.4130
- Luo SF, Zheng DW, Robertson DS, Carter WE (1987) Short-period variations in the length of day: atmospheric angular momentum and tidal components. *J Geophys Res* 92:11657–11661
- Maes C, Sudre J, Garçon V (2010) Detection of the eastern edge of the equatorial Pacific warm pool using satellite-based ocean color observation. *SOLA* 6:129–132. doi:10.2151/sola.2010-033
- Mantua NJ, Hare SR, Zhang Y, Wallace JM, Francis RC (1997) A Pacific interdecadal climate oscillation with impacts on salmon production. *Bull Amer Meteorol Soc* 78:1069–1079
- Morlet J, Arens G, Fourgeau E, Giard D (1982) Wave propagation and sampling theory—part I: complex signal and scattering in multilayered media. *Geophysics* 47:203–221
- Picaut J, Ioualalen M, Menkes C, Delcroix T, McPhaden MJ (1996) Mechanism of the zonal displacements of the Pacific warm pool: implications for ENSO. *Science* 274:1486–1489
- Picaut J, Ioualalen M, Delcroix T, Masia F, Murtugudde R, Vialard J (2001) The oceanic zone of convergence on the eastern edge of the Pacific warm pool: a synthesis of results and implications for El Niño-Southern oscillation and biogeochemical phenomena. *J Geophys Res* 106:2363–2386
- Pierrehumbert RT (1995) Thermostats, radiator fins, and the runaway greenhouse. *J Atmos Sci* 52:1784–1806
- Ramanathan V, Collins W (1991) Thermodynamic regulation of ocean warming by cirrus clouds deduced from observations of the 1987 El Niño. *Nature* 351:27–32
- Rayner NA, Parker DE, Horton EB, Folland CK, Alexander LV, Rowell DP, Kent EC, Kaplan A (2003) Global analyses of sea surface temperature, sea ice, and night marine air temperature since the late nineteenth century. *J Geophys Res* 108:4407. doi:10.1029/2002JD002670
- Ren HL, Jin FF, Stuecker MF, Xie RH (2013) ENSO regime change since the late 1970s as manifested by two types of ENSO. *J Meteorol Soc Japan* 91:835–842
- Saji NH, Goswami BN, Vinayachandran PN, Yamagata T (1999) A dipole mode in the tropical Indian Ocean. *Nature* 401:360–363
- Smith TM, Reynolds RW, Peterson TC, Lawrimore J (2008) Improvements to NOAA's historical merged land-ocean surface temperature analysis (1880–2006). *J Clim* 21:2283–2296. doi:10.1175/2007JCLI2100.1
- Stuecker MF, Timmermann A, Jin FF, McGregor S, Ren HL (2013) A combination mode of the annual cycle and the El Niño/Southern Oscillation. *Nat Geosci* 6:540–544. doi:10.1038/NNGEO1826

- Stuecker MF, Jin FF, Timmermann A, McGregor S (2015) Combination mode dynamics of the anomalous northwest Pacific anticyclone. *J Clim* 28:1093–1111. doi:10.1175/JCLI-D-14-00225.1
- Sun DZ (2003) A possible effect of an increase in the warm pool SST on the magnitude of El Niño warming. *J Clim* 16:185–205
- Thomson D (1982) Spectrum estimation and harmonic analysis. *Proc IEEE* 70:1055–1096
- Uppala SM, Kållberg PW, Simmons AJ, Andrae U, Bechtold VDC, Fiorino M, Gibson JK, Haseler J, Hernandez A, Kelly GA, Li X, ONOGI K, Saarinen S, Sokka N, Allan RP, Andersson E, Arpe K, Balmaseda MA, Beljaars ACM, Berg LVD, Bidlot J, Bormann N, Caires S, Chevallier F, Dethof A, Dragosavac M, Fisher M, Fuentes M, Hagemann S, Hólm E, Hoskins BJ, Isaksen I, Janssen PAEM, Jenne R, McNally AP, Mahfouf JF, Morcrette JJ, Rayner NA, Saunders RW, Simon P, Sterl A, Trenberth KE, Untch A, Vasiljevic D, Viterbo P, Woollen J (2005) The ERA-40 re-analysis. *Q J R Meteorol Soc* 131:2961–3012. doi:10.1256/qj.04.176
- Waliser DE, Graham NE (1993) Convective cloud systems and warm-pool sea surface temperatures: coupled interactions and self-regulation. *J Geophys Res* 98:12881–12893
- Wallace JM (1992) Effect of deep convection on the regulation of tropical sea surface temperature. *Nature* 357:230–231
- Webster PJ, Lukas R (1992) TOGA COARE: the coupled ocean atmosphere response experiment. *Bull Amer Meteorol Soc* 73:1377–1416
- Wyrki K (1975) El Niño—the dynamic response of the equatorial Pacific Ocean to atmospheric forcing. *J Phys Oceanogr* 5:572–584
- Wyrki K (1989) Some thoughts about the west Pacific warm pool. *Proceeding of the Western Pacific International Meeting and Workshop on TOGA COARE*. ORSTUM, New Caledonia, Nouméa, pp. 99–109
- Yan XH, Ho CR, Zheng QA, Klemas V (1992) Temperature and size variabilities of the western Pacific warm pool. *Science* 258:1643–1645
- Yan XH, He Y, Liu WT, Zheng QA, Ho CR (1997) Centroid motion of the western Pacific warm pool during three recent El Niño–Southern Oscillation events. *J Phys Oceanogr* 27:837–845
- Yang S, Ding X, Zheng D, Li Q (2007) Depiction of the variations of Great Plains precipitation and its relationship with tropical central-eastern Pacific SST. *J Appl Meteor Climatol* 46:136–153
- Yeh SW, Kug JS, An SI (2014) Recent progress on two types of El Niño: observations, dynamics, and future changes. *Asia-Pacific J Atmos Sci* 50:69–81
- Yu JY, Kao PK, Paek H, Hsu HH, Hung CW, Lu MM, An SI (2015) Linking emergence of the central Pacific El Niño to the Atlantic multidecadal oscillation. *J Clim* 28:651–662
- Zhang WJ, Li HY, Jin FF, Stuecker MF, Turner AG, Klingaman NP (2015) The annual-cycle modulation of meridional asymmetry in ENSO's atmospheric response and its dependence on ENSO zonal structure. *J Clim* 28:5795–5812
- Zheng DW, Dong DN (1986) Realization of narrow band filtering of the polar motion data with multi-stage filter. *Acta Astronomica Sinica* 27:368–376 (in Chinese)
- Zheng DW, Luo SF (1992) Contribution of time series analysis to data processing of astronomical observations of Earth rotation in China. *Stat Sin* 2:605–618
- Zheng DW, Chao BF, Zhou Y, Yu N (2000) Improvement of edge effect of the wavelet time-frequency spectrum: application to the length of day series. *J Geodesy* 74:249–254
- Zhou YH, Zheng DW (1999) Monte Carlo simulation test of correlation significance levels. *Acta Geodaetica et Cartographica Sinica* 28:313–318 (in Chinese)
- Zhou YH, Zheng DW, Zhao M, Chao BF (1998) Interannual polar motion with relation to the North Atlantic Oscillation. *Glob Planet Chang* 18:79–84